Temperature Sensitivity and Shape Optimization of Solid-State Wave Gyroscopes

Erdal Yilmaz, *Member, IEEE,* and David Bindel, *Member, IEEE*

***Abstract*—We analyze the change of angular gain and vibration frequency of solid-state wave gyroscopes as a result of geometry perturbations due to thermal expansion. We analyze sensitivity of the device to thermal expansion effects by an isoparametric finite element analysis method, and we analyze the sensitivity to thermal changes in the material properties assuming a linear dependence on temperature. We quantify these sensitivities for common device geometries, and use our analysis as the basis for a local optimization problem that minimizes temperature sensitivity as a function of device shape.**

***Index Terms*—gyroscope, solid-state wave, rate-integrating, temperature sensitivity, shape optimization.**

I. Introduction

TEMPERATURE is one of the most important environmental factors affecting gyroscope performance. Temperature variations change both material properties and geometry of resonators. The elastic coefficients of conventional materials used in microfabrication change almost linearly within the standard range of operational temperatures. Also, due to thermal expansion, the device geometry and material density change slightly. Owing to these changes, in harsh operating conditions, like very low or high temperatures, or in the case of a thermal shock, gyroscope parameters drift considerably. For high-performance gyroscope design, it is critical to identify, quantify and control these drifts.

A solid-state wave gyroscope is a particular type of Coriolis Vibratory Gyroscope [1]. Its resonator is an axisymmetric thin shell with degenerate pairs of vibrational modes. The degeneracy is split as a result of coupling by the Coriolis force. A standing wave pattern, formed by the split pair, rotates together with the gyro platform. However, it lags behind by a certain ratio, called Bryan's factor, which is a function of device cross section and vibration mode pair [2], [3]. Based on the orientation of the standing wave, we can measure rotation of the platform. This property holds even if the rotation speed is not constant [4].

As material properties and geometry change due to thermal effects, the frequency, damping and coupling coefficients of vibrations drift [5], [6]. But the temperature induced changes to the shape of an axisymmetric resonator leave the symmetry intact. As a result, the modal frequencies and damping coefficients of the mode pair change together without splitting. Equivalently, we can consider thermal expansion as an axisymmetric imperfection [3]. Because it depends on the geometry of the cross section and Poisson's ratio, Bryan's factor is also affected by thermal expansion.

Designers search for active or passive methods to minimize thermal effects and provide simple calibration procedures. An active control mechanism that keeps the temperature constant, as in oven-controlled crystal oscillators, minimizes drifts at the expense of additional power and requires a well-designed thermal isolation stage [7]. Another mechanism can be constructed by observing changes in some parameters, due to temperature, to compensate for the drifts in others. Frequency based compensation is common in practice utilizing phase locked loops in a feedback circuit [8], [9]. However, a passive control mechanism, like composite material design [10], is desirable, because active control increases mechanical and electrical complexity and thereby the size and power consumption.

Structural shape optimization is another passive control mechanism which can be used to minimize performance degradation due to enviromental factors [11]. Conventional shapes for solid-state wave gyros include rings, cylinders and hemispherical shells. As a result of miniaturization efforts, half-toroidal shells have also been fabricated [12]. These simple shapes allow analytical solutions for gyro related vibration problems and are relatively easy to fabricate. However, there is no *a priori* reason why these shapes would result in robust designs. Based on sensitivity analysis [13], local shape optimization of conventional geometries might improve gyro performance.

The paper is organized as follows. In the next section, we present a lumped model of a solid-state wave gyro and define scale factors for two operation modes. In Section III, we describe the computational details in our simulations. We show how temperature sensitivities can be computed via axisymmetric thermal expansion, and we formulate a local shape optimization problem to minimize the sensitivities. In Section IV, we present our results for conventional geometries. Lastly, we discuss possible geometric improvements.

II. Background

The lumped model of a solid-state wave gyroscope involves two degenerate, coupled, damped and driven harmonic oscillators:

$$\ddot{\mathbf{q}} + 2(\gamma\mathbf{I} + A_g\Omega\mathbf{J})\dot{\mathbf{q}} + \omega^2\mathbf{q} = \mathbf{f} + \boldsymbol{\xi} \tag{1}$$

$$\mathbf{I} \equiv \begin{bmatrix} 1 & 0 \\ 0 & 1 \end{bmatrix}, \quad \mathbf{J} \equiv \begin{bmatrix} 0 & -1 \\ 1 & 0 \end{bmatrix} \tag{2}$$

where the vectors $\mathbf{q}(t)$, $\mathbf{f}(t)$ and $\boldsymbol{\xi}(t)$ correspond to generalized coordinates, drive forces and noise, respectively [14]. ω is the

E. Yilmaz was with Applied Physics, Cornell University, Ithaca, NY, 14853 USA.

D. Bindel is with the Department of Computer Science, Cornell University, Ithaca, NY, 14853 USA.

Manuscript received January 14, 2016; revised January 14, 2016.

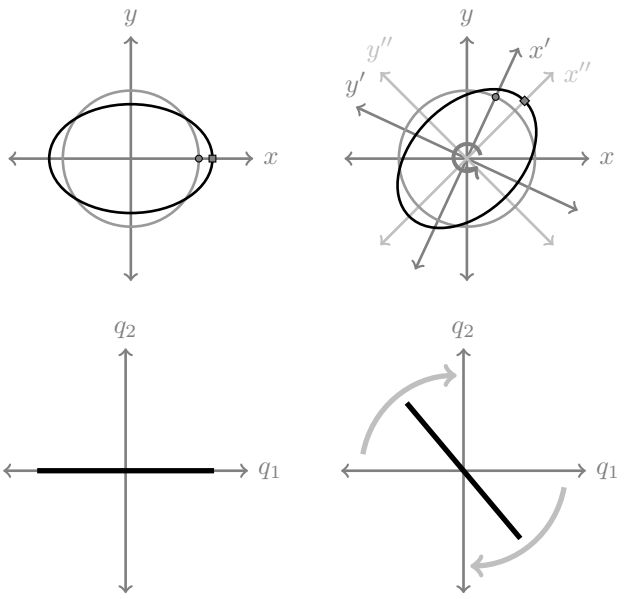

Fig. 1. Wave-inertia effect and operation in rate-integrating mode. Top left: Initial position of standing wave. Top right: (x, y) inertial frame, (x', y') gyroscope frame, (x'', y'') standing wave frame. The device rotates by θ. Standing wave rotates by $(1-\mathcal{B})\theta$. A material point is marked with a circular dot and a point of anti-node of the standing wave is marked with a square dot. Bottom left: Initial position of the linear trajectory. Bottom right: Line rotates by $-A_g\theta$.

undamped angular vibration frequency and Ω is the rotation rate of the gyro platform. $\gamma = \omega/2Q$ is the damping coefficient and Q represents the quality factor. A_g is known as angular gain.

As the device temperature T changes, coefficients of the lumped model drift. Computing $\gamma(T)$, $A_g(T)$ and $\omega(T)$ requires modeling geometric changes of the resonator. In this paper, we focus on computing the last two. The damping coefficient $\gamma(T)$ depends on the relevant damping mechanisms. The most common damping mechanisms are anchor loss, surface loss and thermoelastic dampings. The dominant damping mechanism is design dependent. In this paper, we only provide a formulation for sensitivity of thermoelastic damping; but similar mathematical ideas can be used to compute the sensitivity of other damping effects. We will also leave aside the noise performance which is partly studied for rate mode operation in [15].

The ideal *rate-integrating mode* of operation corresponds to a rotating linear trajectory in the configuration space (q_1, q_2) (Fig. 1) [4]. In fact, it is an ellipse degenerated to a line. When the gyro system rotates by an angle θ around its symmetry axis, the orientation of the linear trajectory rotates by $-A_g\theta$. For a device using vibration modes with azimuthal number m and corresponding Bryan's factor, $\mathcal{B}$:

$$A_g = \mathcal{B} \times m \tag{3}$$

Computation of $\mathcal{B}$ for a general axisymmetric body was previously shown [3].

Solid-state wave gyroscopes may be coupled to control circuitry to compensate for energy loss in rate integrating mode or to maintain the vibration shape in a reference state when

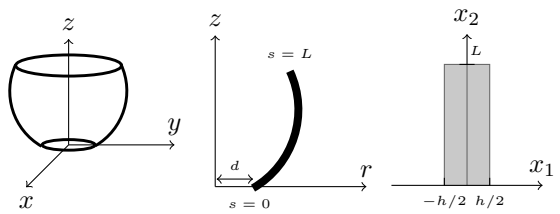

Fig. 2. Left: Axisymmetric shell. Clamped at the bottom boundary, free at the top boundary. Center: Cross section in (r, z)-plane. Right: Computational mapped domain.

operating in rate mode. In either mode, the sensor output is the desired rotation angle or rotation rate times a scale factor that depends on the angular gain A_g and the control circuit transfer function. The angular gain will drift with temperature, resulting in temperature sensitivity of the scale factor. The control circuit also exhibits temperature sensitivity, but we focus on the sensitivity of the mechanical system in this paper.

III. Method

We consider the steady-state temperature distribution of the resonator, the substrate and their environment. By differentiating a linear axisymmetric thermal expansion problem, we compute the sensitivities of gyro parameters to temperature, without solving for the deformation field explicitly. Temperature is treated as a global geometric design parameter.

A. Shell Geometry

Typical solid-state wave gyroscope resonators are axisymmetric shells clamped at one of two boundaries and free on the other (Fig. 2). The cross section of the shell's midsurface forms a plane curve on (r, z)-plane. We parametrize this curve by its arclength, s. We use h, L and d to represent the thickness of shell, the length of midline curve and the distance of the clamped boundary from the symmetry axis respectively. We denote the signed curvature of the midline as $\kappa(s)$.

A plane curve $(r_0(s), z_0(s))$ is fully determined by its curvature $\kappa(s)$ up to a rotation:

$$\frac{d\phi}{ds} = \kappa(s) \tag{4}$$

$$\frac{dr_0}{ds} = \cos(\phi(s)) \tag{5}$$

$$\frac{dz_0}{ds} = \sin(\phi(s)) \tag{6}$$

where $\phi(s)$ is the angle of the tangent to the curve. By integrating the ODE with initial conditions $(\phi(0), d, 0)$ over the range $s \in [0, L]$, we construct a particular curve. Since translation in z-coordinate has no effect on our computations, we put the clamped boundary at the coordinate $(d, 0)$. The free boundary appears at $s = L$.

A standard approach in shape optimization is to use B-spline representation. A special type of spline functions, NURBS, are capable of representing quadratic shapes which are typical in engineering design [16]. For local optimization, we can use the coordinates of NURBS control points as design variables.

For computations, we define a smooth mapping from $(x_1, x_2) \in [-h/2, h/2] \times [0, L]$ to the cross section on (r, z)-plane using the midline coordinates (r_0, z_0):

$$r(x_2) = r_0(x_2) - x_1 \sin(\phi(x_2)) \quad (7)$$

$$z(x_2) = z_0(x_2) + x_1 \cos(\phi(x_2)) \quad (8)$$

For a valid representation, the cross-section should be in the right half-plane ($r \geq 0$) and non-self-overlapping. One of the necessary conditions for the latter is $|\kappa| < 2/h$. Also, if for every point A and B on the midline with $\Delta s > \pi/|\kappa|_{max}$, $|AB| > h$ holds, then these two conditions are sufficient to establish the non-self-overlapping property. Checking these conditions is important if one chooses to generate random curves.

B. Axisymmetric Thermal Deformation

In a material with initial strain $\boldsymbol{\varepsilon}_0$ and initial stress $\boldsymbol{\sigma}_0$, the constitutive relationship is given as:

$$\boldsymbol{\sigma} = \boldsymbol{C} : (\boldsymbol{\varepsilon} - \boldsymbol{\varepsilon}_0) + \boldsymbol{\sigma}_0 \quad (9)$$

where $\boldsymbol{C}$ is the constitutive tensor for linear elasticity; see, e.g. [17, §2.7]. In an isotropic material, thermally induced initial strain is proportional to the temperature change $\Delta T = T - T_0$ and linear thermal coefficient of expansion α_L. In our computations, we did not consider initial stress. Once the shells are released, they are attached only at one boundary, therefore they should not have built-in tension around their free edge where most of the vibration energy is located. If there is some unreleased stress, it will definitely cause problems.

For an axisymmetric expansion, the displacements are non-zero only on the cross section, i.e. $u_\theta = 0$, and two components of strain are zero, $\varepsilon_{r\theta}, \varepsilon_{z\theta} = 0$. After discretizing by finite elements in the standard way, the discretized displacement vector satisfies the matrix equation:

$$\mathbf{K}_T \mathbf{u}_T = \mathbf{f}_T \quad (10)$$

In general, Eq.(10) is nonlinear, as the stiffness matrix and thermal load vectors depend on the deformed geometry, i.e. $\mathbf{K}_T(\mathbf{u}_T)$ and $\mathbf{f}_T(\mathbf{u}_T, T)$. In order to compute temperature sensitivities, we need temperature derivatives of these quantities.

$$\frac{d\mathbf{K}_T}{dT}\mathbf{u}_T + \mathbf{K}_T \frac{d\mathbf{u}_T}{dT} = \frac{d\mathbf{f}_T}{dT} \quad (11)$$

$$\frac{d\mathbf{K}_T}{dT} = \frac{\partial \mathbf{K}_T}{\partial E}\frac{\partial E}{\partial T} + \frac{\partial \mathbf{K}_T}{\partial \nu}\frac{\partial \nu}{\partial T} + \frac{\partial \mathbf{K}_T}{\partial \mathbf{u}_T}\frac{\partial \mathbf{u}_T}{\partial T} \quad (12)$$

$$\frac{d\mathbf{f}_T}{dT} = \frac{\partial \mathbf{f}_T}{\partial T} + \frac{\partial \mathbf{f}_T}{\partial E}\frac{\partial E}{\partial T} + \frac{\partial \mathbf{f}_T}{\partial \nu}\frac{\partial \nu}{\partial T} + \frac{\partial \mathbf{f}_T}{\partial \mathbf{u}_T}\frac{\partial \mathbf{u}_T}{\partial T} \quad (13)$$

For the temperature range of interest (-40C to 85C) the material parameters for common microfabrication materials change linearly. We write Young's modulus and Poisson's ratio as follows: $E(T) = E_0(1 + \alpha_E(T - T_0))$, $\nu(T) = \nu_0(1 + \alpha_\nu(T - T_0))$, where α_E and α_ν are linear thermal coefficients. The room temperature values are $E_0 = E(T_0)$ and $\nu_0 = \nu(T_0)$. The material density also changes as $\rho(T) = \rho_0(1 - 3\alpha_L(T - T_0))$ (Table I).

When the shell is thick enough, i.e. $h/L \gg \alpha_L \Delta T$, the nonlinear effects can be ignored. Besides, in order to compute the temperature sensitivities, we do not need to solve Eq.(10) to find the deformation. The information from the temperature derivative of the shape, $d\mathbf{u}_T/dT$, is sufficient. Hence, we can set $\Delta T = 0$, $\mathbf{u}_T = 0$, and simply compute $d\mathbf{u}_T/dT$ on the original geometry.

$$\frac{d\mathbf{u}_T}{dT} = \mathbf{K}_T^{-1}\frac{d\mathbf{f}_T}{dT} \quad (14)$$

C. Temperature Sensitivities

Due to thermal expansion, the computational domain becomes a function of temperature. Similar to geometric design parameters, we can compute the temperature derivatives of gyroscope parameters, which are basically quantities derived from the finite element matrices. In other words, we can compute the following: $\frac{d\omega}{dT}$, $\frac{d\gamma}{dT}$ and $\frac{dA_g}{dT}$.

For small damping and platform rotations, we can treat the damping and Coriolis terms as perturbations to the original vibration problem:

$$\mathbf{K}\mathbf{u} = \lambda \mathbf{M}\mathbf{u} \quad (15)$$

where $\lambda = \omega^2$. By taking temperature derivatives of both sides we can form a linear system to solve $d\mathbf{u}/dT$ and $d\lambda/dT$:

$$\begin{bmatrix} \mathbf{K} - \lambda\mathbf{M} & -\mathbf{M}\mathbf{u} \\ \mathbf{u}^T & 0 \end{bmatrix} \begin{bmatrix} \mathbf{u}' \\ \lambda' \end{bmatrix} = \begin{bmatrix} \lambda\mathbf{M}'\mathbf{u} - \mathbf{K}'\mathbf{u} \\ 0 \end{bmatrix}. \quad (16)$$

The primed variables stand for temperature derivatives. We also used the normalization constraint $\mathbf{u}^T\mathbf{u}' = 0$.

The temperature derivatives of the finite element matrices can be obtained via isoparametric sensitivity analysis with mesh derivative expressed as the solution of Eq. 14 [13]. We can express temperature sensitivity of frequency as:

$$\frac{1}{\omega}\frac{d\omega}{dT} = \frac{1}{2\lambda}\frac{d\lambda}{dT}. \quad (17)$$

In a similar way, we find the temperature sensitivity of Bryan's factor. For the degenerate vibration modes $\mathbf{u}_1$ and $\mathbf{u}_2$ with azimuthal number m, Bryan's factor is:

$$\mathcal{B} = \frac{b}{2m\mu}, \quad \mu = \mathbf{u}_1^T\mathbf{M}\mathbf{u}_1, \quad b = \mathbf{u}_2^T\mathbf{C}\mathbf{u}_1 \quad (18)$$

where $\mathbf{M}$ and $\mathbf{C}$ are mass and gyroscopic finite element matrices, and

$$\mu' = 2\mathbf{u}_1^T\mathbf{M}\mathbf{u}_1' + \mathbf{u}_1^T\mathbf{M}'\mathbf{u}_1, \quad (19)$$

$$b' = -\mathbf{u}_1^T\mathbf{C}\mathbf{u}_2' + \mathbf{u}_2^T\mathbf{C}'\mathbf{u}_1 + \mathbf{u}_2^T\mathbf{C}\mathbf{u}_1'. \quad (20)$$

Finally, the temperature sensitivity of angular gain can be obtained from that of Bryan's factor:

$$\frac{1}{A_g}\frac{dA_g}{dT} = \frac{1}{\mathcal{B}}\frac{d\mathcal{B}}{dT} = \frac{b'}{b} - \frac{\mu'}{\mu}. \quad (21)$$

The sensitivity of the damping coefficient γ is related to frequency and quality factor:

$$\frac{1}{\gamma}\frac{d\gamma}{dT} = \frac{1}{\omega}\frac{d\omega}{dT} - \frac{1}{Q}\frac{dQ}{dT}. \quad (22)$$

We already showed how to compute the first term. For quality factor, similar temperature derivatives of matrices and vectors

are needed depending on the damping model. In [18], a perturbation approach to compute thermoelastic damping yields the following equations:

$$Q^{-1} = \xi \left|\mathrm{Im} z\right|, \quad \xi = \frac{\chi^2 T}{\rho c_v E}, \quad z = \frac{\mathbf{u}^T \mathbf{K}_{u\theta} \boldsymbol{\theta}}{\mathbf{u}^T \mathbf{K}_{uu} \mathbf{u}}. \tag{23}$$

The oscillating temperature field $\boldsymbol{\theta}$ is solved as a perturbation:

$$(i\omega \mathbf{C}_{\theta\theta} + \eta \mathbf{K}_{\theta\theta})\boldsymbol{\theta} = -i\omega \mathbf{C}_{\theta u} \mathbf{u}. \tag{24}$$

Definitions of constants and finite element matrices involved with Eq. 23–24. can be found in [18]. The sensitivity of quality factor is:

$$\frac{1}{Q}\frac{dQ}{dT} = -Q\frac{d}{dT}(\xi \left|\mathrm{Im} z\right|). \tag{25}$$

D. Simulation Approximations

While performing our simulations, we made some simplifying assumptions. Other than assuming a linear thermal expansion problem and linear temperature dependence of material properties, as mentioned in previous sections, we removed the substrate and post on which the resonator sits from the simulations. We assumed post radius expands with a linear thermal expansion coefficient α_S. The effect of this geometrical change shows itself as a translation in r-direction. The expansion of the post together with the resonator in z-direction can simply be ignored, since z-direction translations do not affect the results. Also, at the clamp position, we let the boundary expand in the thickness direction. This simply constrains u_r and u_z at the clamped boundary to be proportional to distance from the midline, and also $u_r/u_z = -\tan\phi_0$.

E. Shape Optimization

A meaningful cost function is important to any optimization task. Ideally, the cost function for optimizing a gyro would reward high performance and penalize sensitivity to imperfections or temperature variations; but to compute such a cost function, we would need a detailed analysis involving not only the resonator, but also the associated control circuitry. As a first step to demonstrate our approach, we instead use a simpler cost function, and only minimize temperature sensitivity. For example, if we want to minimize the temperature sensitivity of ω and A_g, we can define the following weighted cost function:

$$C(\boldsymbol{\psi}) = w_f(\omega'/\omega)^2 + w_g(A_g'/A_g)^2 \tag{26}$$

where the weights w_f and w_g reflect how much we want to penalize sensitivity of frequency or angular gain, respectively, with constraints:

$$\omega_{min} < \omega < \omega_{max} \tag{27}$$

$$|d\omega/dT| < \omega'_{max} \tag{28}$$

$$A_{gmin} < A_g < A_{gmax} \tag{29}$$

$$|dA_g/dT| < A'_{gmax} \tag{30}$$

and minimize over the space of feasible device cross-sections. We can either search locally, starting with an initial shape and improving it using gradient-based shape optimization, or search globally by randomly generating feasible midline curves.

TABLE I
MATERIAL PROPERTIES AND GEOMETRY OF RESONATORS

Parameter	Symbol	Value
Young's modulus	E_0	$80\,GPa$
Poisson's ratio	ν_0	0.26
Material density	ϕ_0	$2200\,kg/m^3$
Thermal expansion coefficient of resonator	α_L	$1.4 \times 10^{-6}\,K^{-1}$
Thermal expansion coefficient of substrate	α_S	$2.6 \times 10^{-6}\,K^{-1}$
Thermal coefficient of E	α_E	$2.5 \times 10^{-4}\,K^{-1}$
Thermal coefficient of ν	α_ν	$3.0 \times 10^{-4}\,K^{-1}$
Thickness to length ratio	h/L	0.01
Post radius to length ratio (cylindrical)	d_1/L	$12/5\pi$
Post radius to length ratio (spherical)	d_2/L	$12\sin(\pi/12)/5\pi$
Post radius to length ratio (toroidal)	d_3/L	$2/5\pi$
Radius of hemisphere to length ratio	R_2/L	$5\pi/12$
Minor radius of torus to length ratio	R_3/L	$1/\pi$

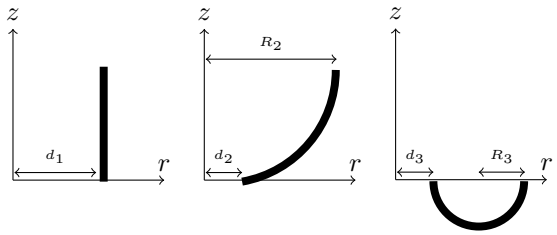

Fig. 3. Left: Cylindrical shell. Center: Truncated hemispherical shell. Right: Half-toroidal shell.

IV. RESULTS

In this section, we present sensitivity computations for certain device geometries and explore design space for improvements. In our simulations we used the spectral element method.

A. Conventional Resonator Geometries

We investigated temperature sensitivities for three common geometries: a cylindrical shell, a truncated hemispherical shell and a half-toroidal shell (Figure 3). They all have the same midline length and shell thickness. We select value of d so that radial extents, r_{max}, are the same. We selected amorphous silicon dioxide ($aSiO_2$) and silicon for the materials of resonator and post respectively. We computed thermal coefficients of elastic properties of $aSiO_2$ from tabulated data provided in [19]. Numerical values used in these simulations are shown in Table I. We are mainly interested in wineglass modes which we identify with their azimuthal number m. These are flexural modes with $2m$ nodal meridians. Simulation results for each shape and azimuthal numbers $m = 2:5$ are tabulated in Tables II, III and IV.

TABLE II
CYLINDRICAL SHELL

m	A_g	$\frac{1}{A_g}\frac{dA_g}{dT}$ $(\frac{ppb}{K})$	ω $(\frac{1}{L}\sqrt{\frac{E_0}{\rho_0}})$	$\frac{1}{\omega}\frac{d\omega}{dT}$ $(\frac{ppm}{K})$
2	0.744	−613	0.345	102.2
3	0.577	−1694	0.214	108.5
4	0.461	−1668	0.159	119.4
5	0.380	−1509	0.161	137.9

TABLE III
TRUNCATED HEMISPHERICAL SHELL

m	A_g	$\frac{1}{A_g}\frac{dA_g}{dT}$ $(\frac{ppb}{K})$	ω $(\frac{1}{L}\sqrt{\frac{E_0}{\rho_0}})$	$\frac{1}{\omega}\frac{d\omega}{dT}$ $(\frac{ppm}{K})$
2	0.554	−305	0.028	108.2
3	0.487	−126	0.061	101.5
4	0.413	−24	0.115	105.0
5	0.353	131	0.182	108.8

TABLE IV
HALF-TOROIDAL SHELL

m	A_g	$\frac{1}{A_g}\frac{dA_g}{dT}$ $(\frac{ppb}{K})$	ω $(\frac{1}{L}\sqrt{\frac{E_0}{\rho_0}})$	$\frac{1}{\omega}\frac{d\omega}{dT}$ $(\frac{ppm}{K})$
2	0.304	−576	0.040	121.6
3	0.357	−220	0.091	110.5
4	0.341	14	0.165	110.5
5	0.311	379	0.252	111.2

Since all thermal coefficients are small, we can write temperature sensitivity of angular gain or frequency as a sum of all effects:

$$y = C_L\alpha_L + C_S\alpha_S + C_E\alpha_E + C_\nu\alpha_\nu \tag{31}$$

where y is either $(1/A_g)dA_g/dT$ or $(1/\omega)d\omega/dT$, and C's are constants for a particular resonator. By setting all α's to zero except one, we can compute the contribution of each thermal effect. Tables V–X show decomposition of these effects for each geometry.

TABLE V
CYLINDRICAL SHELL - THERMAL EFFECT COMPONENTS OF ANGULAR GAIN SENSITIVITY

m	$\frac{1}{A_g}\frac{dA_g}{dT}$ $(\frac{ppb}{K})$	$C_L\alpha_L$	$C_S\alpha_S$	$C_E\alpha_E$	$C_\nu\alpha_\nu$
2	−613	56	−313	0	−356
3	−1694	251	−199	0	−1747
4	−1668	229	−117	0	−1781
5	−1509	178	−70	0	−1618

TABLE VI
CYLINDRICAL SHELL - THERMAL EFFECT COMPONENTS OF FREQUENCY SENSITIVITY

m	$\frac{1}{\omega}\frac{d\omega}{dT}$ $(\frac{ppm}{K})$	$C_L\alpha_L$	$C_S\alpha_S$	$C_E\alpha_E$	$C_\nu\alpha_\nu$
2	102.16	−4.90	0.67	125	−18.6
3	108.48	−7.96	1.05	125	−9.5
4	119.41	−8.38	−0.05	125	2.9
5	137.94	−4.90	−2.62	125	20.5

TABLE VII
TRUNCATED HEMISPHERICAL SHELL - THERMAL EFFECT COMPONENTS OF ANGULAR GAIN SENSITIVITY

m	$\frac{1}{A_g}\frac{dA_g}{dT}$ $(\frac{ppb}{K})$	$C_L\alpha_L$	$C_S\alpha_S$	$C_E\alpha_E$	$C_\nu\alpha_\nu$
2	−305	−105	−269	0	70
3	−126	0	−145	0	18
4	−24	0	−90	0	66
5	131	0	−63	0	194

TABLE VIII
TRUNCATED HEMISPHERICAL SHELL - THERMAL EFFECT COMPONENTS OF FREQUENCY SENSITIVITY

m	$\frac{1}{\omega}\frac{d\omega}{dT}$ $(\frac{ppm}{K})$	$C_L\alpha_L$	$C_S\alpha_S$	$C_E\alpha_E$	$C_\nu\alpha_\nu$
2	108.25	−6.73	0.37	125	−10.3
3	101.55	0.64	−1.06	125	−23.0
4	105.03	0.70	−1.09	125	−19.6
5	108.83	0.70	−1.09	125	−15.8

TABLE IX
HALF-TOROIDAL SHELL - THERMAL EFFECT COMPONENTS OF ANGULAR GAIN SENSITIVITY

m	$\frac{1}{A_g}\frac{dA_g}{dT}$ $(\frac{ppb}{K})$	$C_L\alpha_L$	$C_S\alpha_S$	$C_E\alpha_E$	$C_\nu\alpha_\nu$
2	−576	−4	−441	0	−131
3	−220	0	−231	0	11
4	14	0	−143	0	156
5	379	0	−99	0	477

TABLE X
HALF-TOROIDAL SHELL - THERMAL EFFECT COMPONENTS OF FREQUENCY SENSITIVITY

m	$\frac{1}{\omega}\frac{d\omega}{dT}$ $(\frac{ppm}{K})$	$C_L\alpha_L$	$C_S\alpha_S$	$C_E\alpha_E$	$C_\nu\alpha_\nu$
2	121.63	0.64	−0.28	125	−3.7
3	110.52	0.70	−0.60	125	−14.6
4	110.49	0.70	−0.61	125	−14.6
5	111.19	0.70	−0.61	125	−13.9

Though these results do not show a single common pattern, they nonetheless highlight some critical aspects of the designs. Investigations for particular designs reveal dominant factors and provide intuition for further improvements. For example:

- The cylindrical design is particularly sensitive to Poisson's ratio, and so is more sensitive to temperature variations than the hemispherical and toroidal designs.
- The effect of substrate thermal expansion matter just as much to thermal sensitivity in the other designs, highlighting the importance of selection of the post material and radius.
- However, for $m = 2$, substrate expansion is relatively important to the toroidal shell, and expansion of the resonator is almost irrelevant. The sensitivity to the substrate is greater for the toroidal shell than for the truncated hemisphere, even though the toroidal shell has a smaller anchor; thus, we attribute this effect to the shape itself.
- In general, the $m = 3$ modes are less sensitive to temperature than the $m = 2$ modes, particularly when the substrate effects are minimized. As discussed in [3], the $m = 3$ mode may also be relatively robust to microfabrication imperfections.
- For all devices and modes, angular gain is independent of Young's modulus. Frequency sensitivity depends strongly on thermal variations of Young's modulus, much more than on any geometric effects; hence, new geometries are unlikely to improve frequency sensitivity.

To illustrate how simulation can guide design for lower thermal sensitivity, we consider two design problems. The first one is related to the release of a hemispherical shell resonator

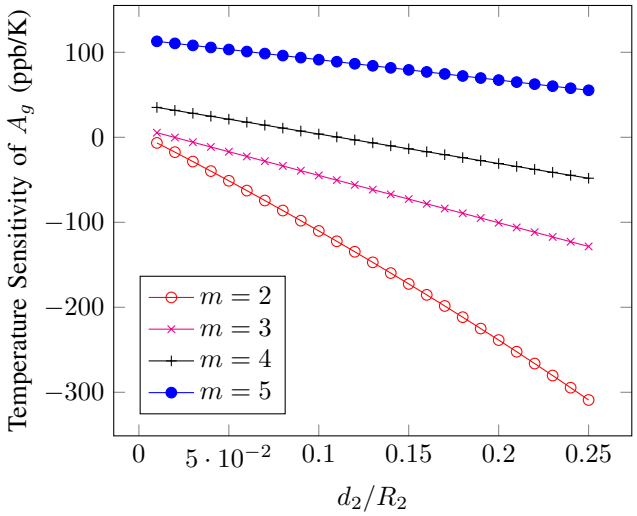

Fig. 4. Temperature sensitivities of angular gain of truncated hemispherical shell as a function of post radius to shell radius ratio. Smaller posts are desirable for $m = 2, 3$ modes. It looks possible to null temperature sensitivity of angular gain for $m = 4$.

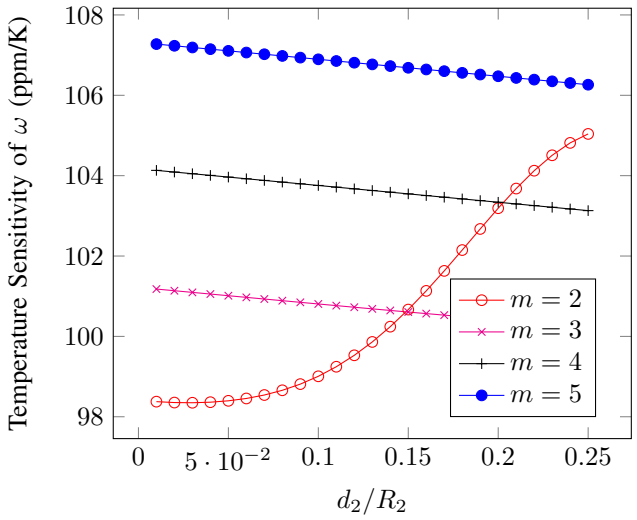

Fig. 5. Temperature sensitivities of frequency of truncated hemispherical shell as a function of post radius to shell radius ratio.

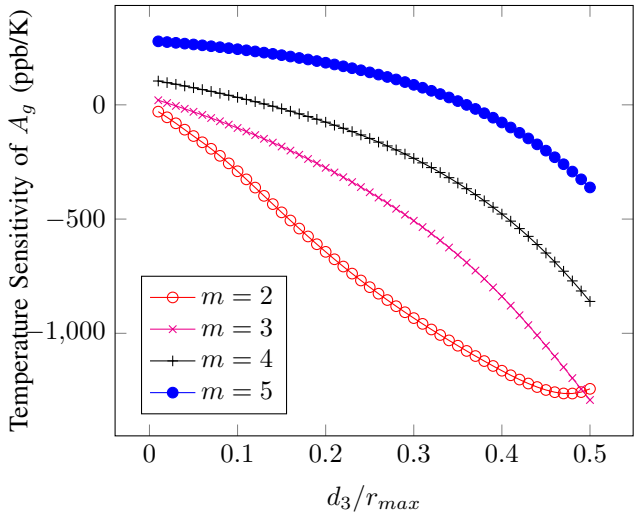

Fig. 6. Temperature sensitivities of angular gain of toroidal shell as a function of post radius to r_{max} ratio. Smaller posts are desirable for $m = 2, 3$ modes. It looks possible to null temperature sensitivity of angular gain for $m = 4, 5$.

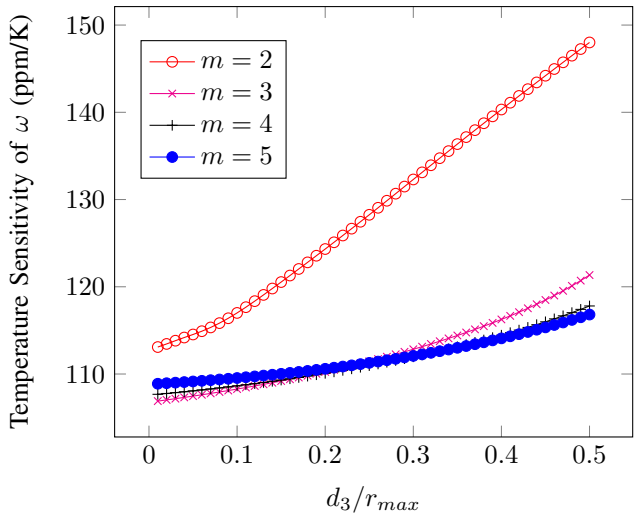

Fig. 7. Temperature sensitivities of frequency of toroidal shell as a function of post radius to r_{max} ratio.

by chemical etching. It is important to stop etching at the right time since it determines the post radius, d_2 (Fig.3). For a constant shell radius, R_2, we swept d_2 value to analyze its effect. We set $h/R_2 = 0.01$ and selected characteristic length as R_2 (Figures 4 and 5).

We observe that the sensitivity of angular gain changes more for the toroidal and hemispherical shells compared to the cylindrical shell.

The second problem involves selecting d_3 and R_3 values for a toroidal geometry with a simple constraint: $d_3 + 2R_3 = r_{max}$. This problem is related to the design of a resonator which encompasses a constant amount of circular area on the chip. We select r_{max} as the characteristic length and keep $h/r_{max} = 0.01$ constant in simulations (Figures 6 and 7).

For both problems we can identify $m = 4$ mode as a good design candidate for minimal temperature sensitivity of angular gain. Also noticable is the high sensitivity of all characteristics of $m = 2$ mode to the design variables.

Finally, we investigated the effect of thickness for both truncated hemisphere and half-toroid shells. Results are shown in Figures 8–11.

B. Gradient-Based Shape Optimization

The main idea of this section is to improve an initial design by deforming the shapes using gradient information. In the previous section, we showed how to optimize temperature sensitivity by sweeping a simple parametric family of standard geometries, such as spheres of varying radius. However, it is usually difficult and sometimes impossible to achieve an optimization goal with only a few design parameters. Standard, simple shapes offer too little flexibility. Instead, we represent the midline curve with NURBS [16], keeping the number of control variables small to simplify the optimization task.

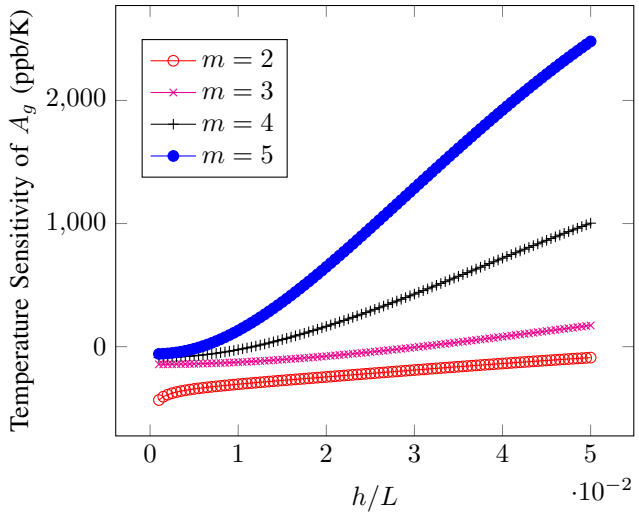

Fig. 8. Temperature sensitivities of angular gain of truncated hemispherical shell as a function of thickness.

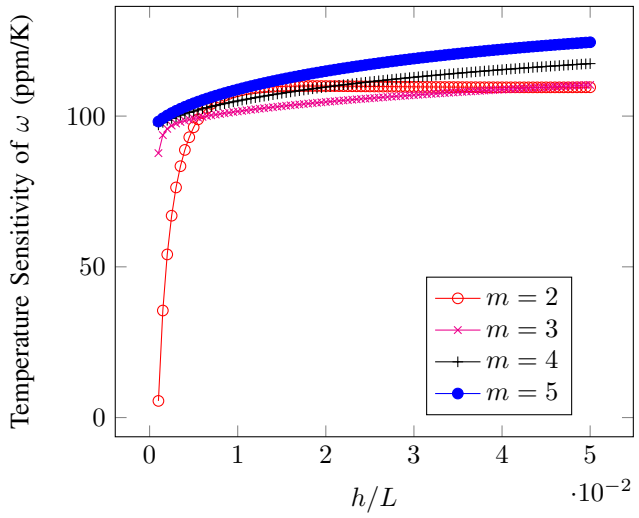

Fig. 9. Temperature sensitivities of frequency of truncated hemispherical shell as a function of thickness.

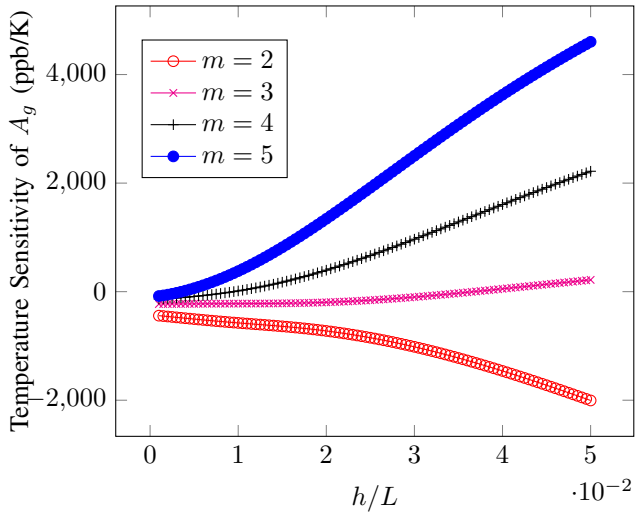

Fig. 10. Temperature sensitivities of angular gain of toroidal shell as a function of thickness.

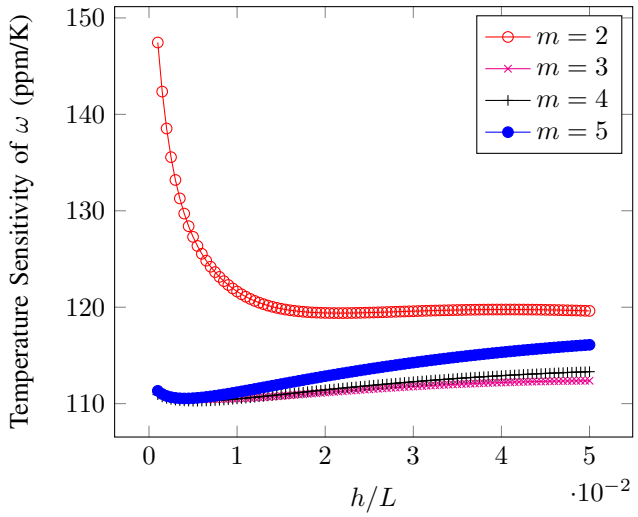

Fig. 11. Temperature sensitivities of frequency of toroidal shell as a function of thickness.

As a simple example, we represent the truncated hemispherical shell with three control points (Fig. 12). The only optimization variables are the coordinates of the middle point; the positions of the points at the clamped and free edges are fixed. Initially, we constrain the motion of our control point to the line connecting its initial position to the center of sphere. In this form, the problem is similar to 1DOF design problems we looked at perviously, and we search for an optimal position on the line with a gradient based method. It is also easy to verify the result a sweeping analysis (Fig. 12). For the subsequent computations, we used an open source nonlinear optimization package [20]. With this particular geometry and materials, we searched an optimal location on the dashed line. We selected the initial position as the origin and the negative direction is towards the spherical center. We searched within a coordinate range of $[-0.35, 0.2]$ on this line. We found null locations for temperature sensitivity of angular gain for modes $m = 2$ and 5. However, it was a monotonically decreasing function of the coordinate along the dashed line for modes $m = 3$ and 4. If we consider contour plots of this function, as a function of (r, z)-coordinates of the middle control point, its zero locations will be possibly be curves. It is less likely to have isolated null points or two-dimensional null regions. During the line search, for $m = 2, 5$ one of those curves intersected the dashed line within our search range providing us with luck. Consequently, we can hope to find an optimal location for $m = 3, 4$ by searching a two dimensional region. We selected a rectangular region as shown in Fig. 13. This selection is a subset of regions where the generated curve can be written a single valued function, $z(r)$. It is convex and an increasing with r. Luckily, we found a null location for mode $m = 4$ (Fig. 13). Gradient search converged to a point on the boundary of the box. When we swept the region, we found that the converged result actually sits inside a valley, which is one of those null curves we mentioned.

Even though a local minimum exist for $m = 3$, it does not improve the sensitivity of the original design by even a factor

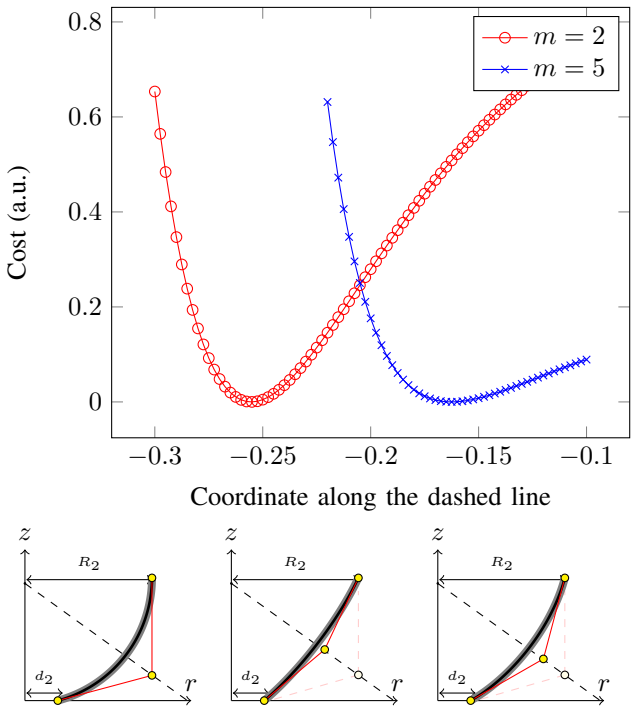

Fig. 12. The simplest shape optimization problem. Bottom left: Three control points representing truncated hemispherical shell. The middle point is free to move along the dashed line while the other two are fixed. Bottom middle and right: Optimal shape and new position of the control point which minimizes temperature sensitivity of angular gain for modes $m = 2$ and $m = 5$ respectively. Top: Local minimum of the cost function for $m = 2$ and $m = 5$ by sweeping the position of control point on the dashed line.

of two. In order to find a null solution for $m = 3$, we could introduce another free control point. Instead, we prefered to use results from previous section as a guideline. We found that the effect of the substrate is considerable, so we let the control point at the clamp to move in the r direction within a box constraint, $[0, d_2]$. This finally resulted in a null for $m = 3$.

The more control points we have, the better we can control the shape. However, this results in solving a higher dimensional optimization problem. As an example, we demonstrate local optimization of toroidal shell problem with two representations, with 5 and 9 control points, respectively (Fig. 14). As in the case of the hemispherical shell, it is possible to represent the initial geometry perfectly using quadratic NURBS. However, if the control points are allowed to move without constraints, the resulting spline may fail to be twice differentiable, which we do not want. We can address this problem in one of two ways. We can constrain the knot locations, e.g. forcing the three inner points to be co-linear in the five point case (for C^1 continuity) and matching curvature at the middle point. This reduces the number of effective degrees of freedom from 6 to 4 in the 5-point case, and from 14 to 8 in the 9-point case. A simple alternative is to use higher-order NURBS functions (at least two higher than the maximum knot multiplicity), which leaves the optimization problem free from equality constraints. In Figure 14, we show two shape improvements for $m = 2$.

As we have seen with the previous examples, even for a simple cost function without many constraints, it can be

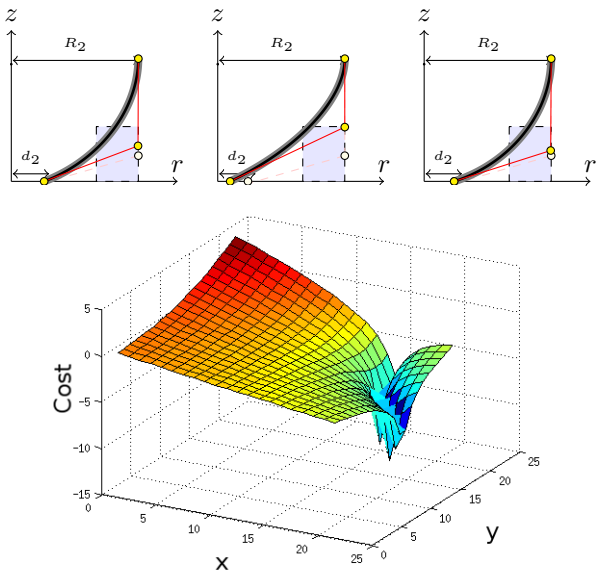

Fig. 13. Left: 2DOF optimization. The middle point is free to move in a 2D rectangular region. Optimal shape and position shown for $m = 4$. Middle and right: 3DOF optimization. Control point at the clamp is also free to move in radial direction. Optimal shapes and positions for $m = 3$ and $m = 4$ respectively. Bottom: Surface plot of the logarithm of cost function corresponding to the 2DOF problem. The shaded region is divided into 25 steps in (r, z)-directions. (x, y)-indices correspond the location of the control point within this design space. In the valley, the temperature sensitivity of angular gain is zero.

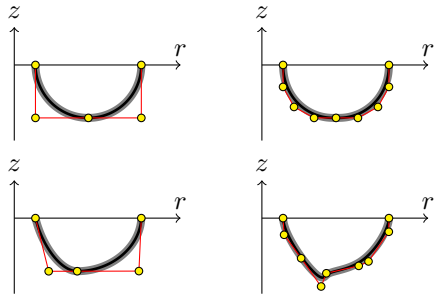

Fig. 14. Top: Two representations of a toroidal shell with 5 and 9 control points corresponding to a quadratic and a quartic NURBS. Bottom: Improved shapes for $m = 2$.

challenging to find an optimal solution. So far, we just used $w_f = 0$ and $w_g \neq 0$ with box or linear constraints. Adding new degrees of freedom helped us achieve design goals in otherwise impossible situations. Control points allowed us to define free form shapes. Still, we only sought a local optimum starting from a familiar initial geometry.

The next obvious question we can ask is whether there is a different geometry which brings together many desirable qualities at once. One can attempt to answer such a question by randomly searching the space of all possible curves. Since we did not have many realistic performance measures, we did not go into this direction.

V. Discussion

The analysis in this paper demonstrates our computational approach, but in practical applications it is important to con-

sider features other than temperature sensitivity. For example, even though post radius can form a good design variable to minimize temperature sensitivity of angular gain, we know that larger posts will in general result in lower quality factors. Also, operating in the $m = 4$ mode may require more electrodes than other modes, and the resulting design may be more strongly affected by microfabrication imperfections [3]. From this perspective, the $m = 3$ mode with a small post may be preferable. In addition, we have reported linear sensitivity at a fixed operating temperature. Linear sensitivity analysis is less expensive than sweeping the temperature. But variations with temperature may not be linear over the whole temperature range, either because of geometry variations or because of nonlinear dependence of material parameters on temperature. We leave a more complete investigation of nonlinear effects to future work.

VI. Conclusion

We showed that temperature sensitivity of angular gain is an additive component to scale factor sensitivity. Starting from linear thermal expansion, we computed temperature sensitivities of both angular gain and vibration frequency. We analyzed conventional geometries and decomposed sensitivities into thermal effects due to resonator expansion, post expansion and change of material properties. We discovered that thermal effects can compensate each other and through simple geometrical design we can null angular gain sensitivity. We also showed how gradient based shape optimization techniques can be used to improve performance.

Acknowledgment

The authors would like to thank DARPA MRIG program for support.

References

[1] *IEEE Standard Specification Format Guide and Test Procedure for Coriolis Vibratory Gyros*, Std., Dec 2004.
[2] G. H. Bryan, "On the beats in the vibrations of a revolving cylinder or bell," *Proceedings of the Cambridge Philosophical Society*, vol. 7, pp. 101–111, 1890.
[3] E. Yilmaz and D. Bindel, "Effects of imperfections on solid-wave gyroscope dynamics," in *SENSORS, 2013 IEEE*, Nov 2013, pp. 1–4.
[4] V. Zhuravlev, "Theoretical foundations of solid-state wave gyroscopes," *Mechanics of Solids*, vol. 28, pp. 3–15, 1993.
[5] V. Dzhashitov and V. Pankratov, "Mathematical models of the thermoelastic stress-strain state, temperature, and technological errors of a wave solid-state sensor of inertial information," *Journal of Machinery Manufacture and Reliability*, vol. 39, no. 3, pp. 248–255, 2010. [Online]. Available: http://dx.doi.org/10.3103/S1052618810030076
[6] C. C. Painter and A. M. Shkel, "Structural and thermal modeling of a z -axis rate integrating gyroscope," *Journal of Micromechanics and Microengineering*, vol. 13, no. 2, p. 229, 2003. [Online]. Available: http://stacks.iop.org/0960-1317/13/i=2/a=310
[7] S. H. Lee, J. Cho, S. Lee, M. F. Zaman, F. Ayazi, and K. Najafi, "A low-power oven-controlled vacuum package technology for high-performance mems," in *Micro Electro Mechanical Systems, 2009. MEMS 2009. IEEE 22nd International Conference on*, Jan 2009, pp. 753–756.
[8] I. P. Prikhodko, A. A. Trusov, and A. M. Shkel, "Compensation of drifts in high-Q MEMS gyroscopes using temperature self-sensing," *Sensors and Actuators A: Physical*, vol. 201, no. 0, pp. 517 – 524, 2013. [Online]. Available: http://www.sciencedirect.com/science/article/pii/S0924424712007613
[9] X. Wang, W. Wu, Z. Fang, B. Luo, Y. Li, and Q. Jiang, "Temperature drift compensation for hemispherical resonator gyro based on natural frequency," *Sensors*, vol. 12, no. 5, pp. 6434–6446, 2012. [Online]. Available: http://www.mdpi.com/1424-8220/12/5/6434
[10] R. Melamud, S. A. Chandorkar, B. Kim, H. K. Lee, J. Salvia, G. Bahl, M. Hopcroft, and T. Kenny, "Temperature-insensitive composite micromechanical resonators," *Microelectromechanical Systems, Journal of*, vol. 18, no. 6, pp. 1409–1419, Dec 2009.
[11] S. J. O. M. Hinton, E., *Analysis and optimization of prismatic and axisymmetric shell structures : theory, practice, and software*. London; New York: Springer, 2003.
[12] J. Cho, J. Yan, J. A. Gregory, H. Eberhart, R. L. Peterson, and K. Najafi, "High-*Q* fused silica birdbath and hemispherical 3-D resonators made by blow torch molding," in *Proc. IEEE MEMS*, 2013, pp. 177–180.
[13] J. Haslinger and R. A. E. Makinen, *Introduction to Shape Optimization*. Society for Industrial and Applied Mathematics, 2003. [Online]. Available: http://epubs.siam.org/doi/abs/10.1137/1.9780898718690
[14] E. Yilmaz, "Design, analysis and simulation of microscale solid-wave gyroscopes," Ph.D. dissertation, Cornell University, 2016.
[15] R. Leland, "Mechanical-thermal noise in mems gyroscopes," *Sensors Journal, IEEE*, vol. 5, no. 3, pp. 493–500, June 2005.
[16] L. A. Piegl and W. Tiller, *The Nurbs Book*. Springer, 1995.
[17] T. J. R. Hughes, *The Finite Element Method*. Dover Publications, 2000.
[18] D. Bindel, "Structured and parameter-dependent eigensolvers for simulation-based design of resonant mems," Ph.D. dissertation, UC Berkeley, 2006.
[19] A. Polian, D. Vo-Thanh, and P. Richet, "Elastic properties of a-sio 2 up to 2300k from brillouin scattering measurements," *EPL (Europhysics Letters)*, vol. 57, no. 3, p. 375, 2002. [Online]. Available: http://stacks.iop.org/0295-5075/57/i=3/a=375
[20] S. G. Johnson, "The nlopt nonlinear-optimization package, http://ab-initio.mit.edu/nlopt."

Erdal Yilmaz Erdal Yilmaz received the Ph.D. degree in applied and engineering physics from Cornell University in 2016, and currently works at Analog Devices in Boston. His research interests include physical simulation and MEMS design.

David Bindel David Bindel received the Ph.D. degree in computer science from UC Berkeley in 2006, and was subsequently a Courant Instructor of Mathematics at NYU. He is currently an Assistant Professor of Computer Science at Cornell University in the Department of Computer Science. His research is focused on simulation, numerical linear algebra, and optimization applied to problems from engineering and computer science.